Insights on the relevance of DFT+U formalism for strongly correlated Ta d electrons probing the nanoscale in oxides: Combined time-differential perturbed γ-γ angular correlation spectroscopy and *ab initio* study in ^{181}Hf($\rightarrow$ ^{181}Ta)-implanted α-Al$_2$O$_3$ single crystal

G. N. Darriba [1,*], R. Faccio [2], P.-D. Eversheim,[3] and M. Rentería [1,†]

[1]*Departamento de Física and Instituto de Física La Plata [IFLP, Consejo Nacional de Investigaciones Científicas y Técnicas (CONICET) La Plata], Facultad de Ciencias Exactas, Universidad Nacional de La Plata, CC 67, 1900 La Plata, Argentina*
[2]*Área Física, DETEMA, Facultad de Química, Universidad de la República, Gral. Flores 2124, P.O. Box 1157, Montevideo, Uruguay*
[3]*Helmholtz-Institut für Strahlen- und Kernphysik (ISKP), Universität Bonn, Nussallee 14–16, 53115 Bonn, Germany*

This work presents a combined experimental and *ab initio* study investigating the relevance of applying the density-functional theory plus U (DFT+U) formalism to correctly describe strongly correlated electrons of diluted probe atoms useful to sense the nanoscale in any material, in particular, 5d orbitals of ^{181}Ta probe atoms doping insulating and semiconducting oxides. Experimentally, we applied the time differential perturbed γ-γ angular correlation (TDPAC) spectroscopy using ion-implanted ^{181}Hf($\rightarrow$ ^{181}Ta) tracers in parts per million concentration in an α-Al$_2$O$_3$ single crystal, measuring the hyperfine interactions (HFIs) for a complete key set of crystal orientations, achieving the observation of the desired axially symmetric electric-field gradient tensor (EFG) sensed by substitutional ^{181}Ta atoms at Al sites *free of defects*. This goal allowed a direct comparison of a known physical situation with the correct first-principles modeling. The all-electron *ab initio* electronic structure calculations were performed in the framework of DFT and DFT+U formalisms. A complete defect-formation energy study for different charge states of the doped systems was essential to determine the correct ionization degree of the Ta impurity, which is likely to be double ionized already at room temperature, showing also the necessity to apply the Hubbard U parameter to correctly describe the electron density and electronic structure of the strongly localized Ta-5d states as ^{181}Ta acts as an isolated probe impurity in α-Al$_2$O$_3$. This combined study also permitted to assign the second observed HFI to ^{181}Ta atoms at substitutional Al sites with structural disorder in their distant neighborhood. We show that the inclusion of the U parameter does not produce significant changes in the equilibrium atomic positions, indicating that all the changes produced in the EFG come from the electron density recombination, showing the extraordinary capability of the EFG to detect subtle changes in the electronic structure. We also show that the Ta-d contribution to the EFG is dominant over the p one, decreasing as the impurity level becomes ionized. When this level is empty, the Ta-p contribution is the dominant one, leading to the experimentally observed EFG. The necessity to apply the DFT+U formalism at Ta probe atoms in semiconductors and insulators to correctly describe the EFG tensor is discussed, proposing that the use of DFT+U becomes relevant only when the probe´s impurity level is strongly localized.

I. INTRODUCTION

To study the influence of doping impurities in condensed matter and the development of new functional materials, nowadays it is crucial to perform combined experimental and accurate theoretical studies of electronic and structural basic properties of the impurity-host system. Among semiconducting oxide materials, doping them with metal impurities may lead to unexpected physical properties (see, e.g., Refs. [1–17]).

At a subnanoscopic level, it is possible to obtain valuable information about key physical properties in doped systems, at the atomic level and also bulk properties, combining precise experimental determinations of the electric-field gradient (EFG) tensor at a given impurity probe-atom site [18] with all-electron *ab initio* electronic structure calculations in the framework of the density-functional theory (DFT) [19,20]. Experimental nuclear solid-state techniques, such as the time-differential perturbed γ-γ angular correlation (TDPAC) spectroscopy [21], can provide high-precision determinations of the EFG tensor, measuring the hyperfine interaction (HFI) between the nuclear quadrupole moment of a suitable probe nucleus and the EFG at this site. From the point of view of *ab initio* calculations, some methods are implemented to describe the electronic structure and charge density $\rho(\mathbf{r})$ in impurity-host crystalline systems. In particular, the full-potential augmented plane-wave plus local orbitals (FP-APW + lo) method [22] describes very accurately $\rho(\mathbf{r})$ in the close neighborhood of a given atomic nucleus, providing a correct prediction of the EFG tensor at this atomic position. The high sensitivity of the EFG tensor to subtle variations in the asymmetry of $\rho(\mathbf{r})$ very close to the probe nucleus when using

*darriba@fisica.unlp.edu.ar
†renteria@fisica.unlp.edu.ar

this combined study enables one to obtain very precise and valuable information about the local environment of the probe atom and of the whole material. That is, due to the strong correlation between the EFG and $\rho(\mathbf{r})$ in a given physical system, the agreement between the experimental EFG and the predicted one validates the description of $\rho(\mathbf{r})$ and therefore all the ground-state properties, converting the EFG and this double-experimental and theoretical approach in a powerful tool in the study of impurities in condensed-matter physics.

Nevertheless, the simple agreement between the measured and calculated EFG does not assure that we have the correct $\rho(\mathbf{r})$ since we are dealing with an impurity. In effect, since the impurity-host system can be in different charge states, the precedent agreement must come from the system with the charge state with the lowest defect formation energy. In this sense, the principal motivation of this work was to give insights on the correct description of $\rho(\mathbf{r})$ due to the presence of strongly correlated impurity´s states in oxides, thanks to the high sensitivity of the EFG on $\rho(\mathbf{r})$ at the atomic level. Specifically, to answer the question of when it is relevant and necessary to use the DFT+U formalism in the impurity treatment. Therefore, as $(^{181}\text{Hf} \rightarrow)^{181}\text{Ta}$ is one of the most used TDPAC probes and it has strongly correlated 5d states, we chose for this purpose to study $^{181}\text{Hf}(\rightarrow \, ^{181}\text{Ta})$-doped α-Al$_2O_3$, a semiconducting wide band-gap oxide with native cations that presents the advantage of not having strongly correlated electrons.

The TDPAC technique using the ^{181}Ta probe atom has been systematically applied to binary oxides belonging to different crystalline groups (*bixbyite, rutile, corundum*, etc.) [23–38], but only in very few cases the combined experimental-DFT approach was used (see, e.g., Refs. [38–43]) to investigate local and bulk structural, electronic, and magnetic properties in these doped materials. In none of these works was the DFT+U formalism applied and only in some of them was the *ab initio* defect-formation energy study performed [40,41].

With respect to the selected system, Rentería *et al.* [44] have already reported a combined study in $^{181}\text{Hf}(\rightarrow \, ^{181}\text{Ta})$-doped α-Al$_2O_3$ single crystal using TDPAC spectroscopy and the full-potential linearized-augmented plane-wave (FP-LAPW) method. Nevertheless, this work presented some controversial results and particularities, both in the experiments and in the calculations, which did not allow to find the expected axially symmetric EFG related to ^{181}Ta probes located at the substitutional defect-free Al site in α-Al$_2$O$_3$, nor the correct assignment of the observed HFIs.

From the experimental point of view, in that work the ^{181}Hf-implanted single crystal was annealed 1 h at 1073 K and then 1 h at 1173 K. After the first annealing only two measurements were performed, both corresponding to different positions with the [001] axis, and therefore V_{33} (the largest component of the EFG tensor), perpendicular to the detector's plane, and thus obtaining basically the same spectra, fitted with one HFI1 characterized by $V_{33} = 11.3(2) \times 10^{21}$ V/m^2 in the [001] crystal direction and an asymmetry parameter $\eta = 0.20(2)$. After the second annealing, a complete set of measurements as a function of the orientation of the single crystal was performed, both with the [001] axis (and V_{33}) perpendicular and parallel to the detector's plane. Here, the already observed HFI1 diminished its population to 40% and

a second distributed HFI2 appeared with a population of 60%, characterized by $V_{33} = 18.4(4) \times 10^{21}$ V/m^2, $\eta = 0.71(5)$, and with *polycrystalline character*. Unfortunately, no measurements were done before the second annealing with V_{33} parallel to the detector's plane, where the spectra are very sensitive to the direction of V_{33} with respect to the detectors, providing key information that would have made possible to identify a hidden fraction of probes localized at *defect-free* Al sites producing an axially symmetric EFG.

With respect to the *ab initio* predictions, the calculations made with the FP-LAPW method at that time have some weak points from the methodological point of view:

(i) The impurity dilution achieved at that time did not represent the experimental condition of an isolated impurity.

(ii) Defect-formation energy studies were not performed, not enabling to know the most probable charge state of the doped system (i.e., the ionization degree of the impurity).

(iii) The precedent facts and the described problem with the annealing in the experiment led to a fortuitous agreement between the *ab initio* prediction and the reported experimental V_{33}, given an erroneous characterization of the HFI observed.

(iv) In addition, a complete electronic study of the doped system analyzing the electronic structure and density to understand the behavior and origin of the EFG was not performed.

For all this, in this work we report results combining dedicated key TDPAC experiments at highly dilute (parts per million, ppm) $(^{181}\text{Hf} \rightarrow)^{181}\text{Ta}$ probes doping an α-Al$_2$O$_3$ single crystal in a wide set of crystal orientations, and a complete *ab initio* electronic structure calculation study using both DFT and DFT +U formalisms. Based on the fact that after an annealing at 1173 K, Rentería *et al.* observed an unexpected HFI with polycrystalline character, not assignable to ^{181}Ta probes located substitutionally at Al cation sites, all measurements reported here were performed after a careful set of thermal treatments up to the limit value of 1073 K with the aim to achieve an axially symmetric HFI characterizing ^{181}Ta atoms localized substitutionally at free of defects Al sites in the *corundum* structure. On the other hand, the *ab initio* calculations were performed using two methods with different approaches, the FP-APW + lo [22] and the projector-augmented wave (PAW) [45,46], strategy that allowed us to study very large supercells to guarantee total convergence of the hyperfine parameters as a function of the supercell (SC) size for all the studied systems (i.e., for the different charge states of the doped systems). This study warrants a reliable modeling of the experimental condition of an isolated impurity, which is strictly necessary for an accurate comparison with this kind of experiment. To correctly assign the observed HFIs we also performed the *ab initio* study of the defect-formation energy for each charge state of the doped system. To treat the electronic correlations in the Ta probe-atom's neighborhood we used also the DFT+U formalism [47–49], adding the Hubbard U parameter to correctly describe the electronic localization of Ta-5d states. The inclusion of the U parameter in the literature to account for the strong Coulomb interaction of Ta-d electrons has been performed in the study of the electronic structure and structural atomic properties on a couple of Ta compounds [50] and when, in particular, the research was focused on the energy band gap [51]. In these works, the Ta atoms are constituents of the compounds,

playing an essential role in the physical magnitudes studied. In our case, the situation is completely different. The Ta atom is an *isolated impurity* and, more importantly, it is the probe atom that *senses* the EFG. Up to now this formalism was not applied to the case of the ^{181}Ta atom acting as an isolated probe impurity. With this formalism, comparing the experimental and predicted EFG tensor and considering the defect-formation energy study, we will demonstrate the necessity to include the U parameter to correctly describe the highly localized Ta-d states to accurately predict the EFG tensor and to assign the HFIs experimentally observed. Also, we will discuss why in previous studies in Ta-doped rutile TiO_2 [39] and SnO_2 [40], where a DFT+U study was not performed, the inclusion of the U parameter to treat the Ta-5d states is irrelevant in the study of the EFG tensor.

This paper is organized as follows. In Sec. II we present the TDPAC spectroscopy, and the perturbation factor used to analyze the spectra coming from single-crystalline samples. Then, a description of the sample, experimental setup, and results are presented. In Sec. III we describe the *ab initio* procedure and calculation details. The theoretical predictions for the structural and electronic properties, the EFG tensors, and the impurity-formation energies for all the charge states studied are presented and discussed in this section in terms of both DFT and DFT+U formalisms. In Sec. IV, we compare and discuss the experimental results and the *ab initio* EFG predictions, performing the final assignment of the HFIs experimentally determined. Finally, in Sec. V we present our conclusions.

II. EXPERIMENT

A. TDPAC spectroscopy and data reduction for single-crystalline samples

The TDPAC spectroscopy measures the perturbation generated by extranuclear fields on the angular correlation between the $\boldsymbol{k}_1$ and $\boldsymbol{k}_2$ directions of two successive γ rays (γ_1 and γ_2) emitted during a nuclear γ-γ decay cascade of a given radioactive probe atom. A complete description of the TDPAC technique can be found in Refs. [21,52]. In the case of electric-quadrupole interactions, this perturbation is originated by the interaction between an extranuclear EFG and the nuclear quadrupole moment (Q) of the intermediate nuclear state (I) of the γ-γ cascade, producing the splitting of this nuclear level. In this work we use the $I = +5/2$ intermediate state of the 133–482-keV γ-γ cascade of ^{181}Ta probes, produced after the β^- nuclear decay of the ^{181}Hf isotope. For $I = +5/2$ and a nonzero EFG, the nuclear level I is split in three double-degenerated m sublevels separated by $\hbar\omega_i$, where the ω_i are the interaction frequencies ($i = 1, 2, \omega_1 \leqslant \omega_2$, and $\omega_3 = \omega_1 + \omega_2$). The emission anisotropy of γ_2 once γ_1 is emitted is modulated periodically by the time evolution of the population of each sublevel. Experimentally, this modulation is determined measuring the number of coincidence events $C(\Theta, t)$ in which a γ_2 ray is detected at an angle Θ with respect to $\boldsymbol{k}_1$ at a time t after the γ_1 detection. The four coplanar detectors used in our experimental setup are located at the standard angular positions $\Theta = 180°$ and $\Theta = 90°$. Hence, the experimental asymmetry ratio or $R(t)$ TDPAC spectrum

is constructed as [27]

$$R(t) = 2\frac{W(180°) - W(90°)}{W(180°) + 2W(90°)} \cong A_{22}^{\exp} G_{22}(t), \quad (1)$$

with $W(\Theta, t)$ the experimental coincidences $C(\Theta, t)$ corrected for accidental counts, taking into account the equivalent detections between detectors separated at an angle $\Theta = 90°$ and $\Theta = 180°$. Here, $A_{22}^{\exp}$ is the effective anisotropy of the γ-γ cascade and $G_{22}(t)$ the multiple-site theoretical perturbation factor, which for nuclear electric-quadrupole interactions and $I = +5/2$ takes the form

$$G_{22}(t) = \sum_i f_i \left[S_{20_i} + \sum_{n=1}^{3} S_{2n_i} \cos(\omega_{n_i} t) \exp(-\delta_i \omega_{n_i} t) \right], \quad (2)$$

having all the information of the hyperfine interaction for each fraction f_i of nuclei experiencing a certain EFG. The nuclear quadrupole frequency $\omega_Q = eQV_{33}/4I(2I-1)\hbar$ is related to the ω_n interaction frequencies by $\omega_n = g_n(\eta)\,\omega_Q$, where the g_n coefficients are known functions [53] of the asymmetry parameter $\eta = (V_{11} - V_{22})/V_{33}$. The V_{ii} are the principal components of the diagonalized EFG tensor, arbitrarily chosen as $|V_{33}| \geqslant |V_{22}| \geqslant |V_{11}|$. Being traceless due to the validity of the Laplace equation at the nucleus, the EFG tensor is completely defined by only two parameters, ω_Q and η. The S_{2n} ($n = 1,2,3$) coefficient is the amplitude of the oscillating contribution with ω_n frequency while S_{20} gives a constant contribution to the perturbation function, where S_{2n} ($n = 0,1,2,3$) are normalized. The exponential functions in Eq. (2) account for a Lorentzian frequency distribution of relative width δ around ω_n.

The hyperfine parameters can be then extracted by fitting the function

$$R(t)^{\text{fit}} = A_{22}^{\exp} G_{22}^{\exp}(t) \quad (3)$$

to the experimental $R(t)$ spectrum, where $G_{22}^{\exp}(t)$ is the convolution of the theoretical perturbation factor $G_{22}(t)$ of Eq. (2) with the time-resolution curve of the spectrometer.

In the case of polycrystalline samples, the S_{2n} ($n = 1,2,3$) coefficients of Eq. (2) only depend on η. However, in the case of single crystals, these coefficients and S_{20} also depend on the relative orientation of the principal axes of the EFG with respect to the emission directions $\boldsymbol{k}_1$ and $\boldsymbol{k}_2$ of the two γ rays, with a set of coefficients existing for each crystal orientation (i.e., for each orientation of the EFG) with respect to the detector´s coordinate system. To determine these coefficients, the perturbation function $R(t)^{\text{fit}} = A_{22}^{\exp} G_{22}^{\exp}(t)$ of Eq. (3) was fitted to each $R(t)$ spectrum, letting free the S_{2n} coefficients of Eq. (2) (called S_{2n}^{free}) during the fitting procedure, determining in consequence one set of S_{2n}^{free} coefficients for each single-crystal orientation [39]. The EFG tensor orientation with respect to the crystalline axes can be extracted by comparing the experimental S_{2n}^{free} and the calculated S_{Kn}^{eff} coefficients:

$$S_{Kn}^{\text{eff}}(\eta) = \frac{2}{3}[S_{Kn}(180°, \eta) - S_{Kn}(90°, \eta)], \quad (4)$$

where

$$S_{Kn}(\boldsymbol{k}_1, \boldsymbol{k}_2, \eta) = \left[S_{22}^n(\boldsymbol{k}_1, \boldsymbol{k}_2, \eta) + \frac{A_{42}}{A_{22}} S_{42}^n(\boldsymbol{k}_1, \boldsymbol{k}_2, \eta) \right]. \quad (5)$$

The $S_{22}^n(\boldsymbol{k}_1, \boldsymbol{k}_2, \eta)$ and $S_{42}^n(\boldsymbol{k}_1, \boldsymbol{k}_2, \eta)$ coefficients of Eq. (5) were obtained using the formalism presented in Ref. [54], with $\boldsymbol{k}_1$ and $\boldsymbol{k}_2$ denoting the coefficient dependence on the orientation between $\boldsymbol{k}_1$ and $\boldsymbol{k}_2$ and the principal axes system of the EFG tensor. Due to the angular configuration of the experimental setup, Eq. (5) must be evaluated for both angles $\Theta = 90°$ and $\Theta = 180°$ between $\boldsymbol{k}_1$ and $\boldsymbol{k}_2$ (i.e., for each angle between pairs of scintillators detecting γ_1 and γ_2) once the relative orientation of the EFG tensor with respect to the detector´s coordinate system has been proposed. For a certain EFG orientation with respect to the detector´s system, Eq. (5) must be averaged over the two inequivalent detections of γ_1 and γ_2 for detectors positioned at $\Theta = 180°$, and also for $\Theta = 90°$, to construct the S_{Kn}^{eff} coefficients of Eq. (4).

In summary, since the orientation of the crystalline axes in a single crystal can be determined independently by diffraction experiments, and given that the agreement between S_{2n}^{free} and S_{Kn}^{eff} enables to determine the orientation of the EFG tensor with respect to the detector's system (i.e., also with respect to the single-crystalline sample), hence the EFG orientation with respect to the crystalline axes can be determined by this methodology.

B. Sample description, experimental setup, and TDPAC measurements

The TDPAC experiments were carried out using the intermediate nuclear state ($I = +5/2$, $\tau_{1/2} = 10.8$ ns) of the 133–482-keV γ-γ cascade of the ^{181}Ta probe, which is populated through the β^- process of the ^{181}Hf nuclear decay. Commercial (99.99% purity) $10 \times 10 \times 0.5$-mm^3 α-Al$_2$O$_3$ single crystal was implanted with ^{181}Hf$^+$ ions at room temperature (RT) at the Bonn Ion Separator and Implanter BONIS facility of the Helmholtz-Institut für Strahlen- und Kernphysik (H-ISKP) at Bonn University (Germany) with an energy of 160 KeV and a dose of 10^{13} ions per cm^2, into the 10×10-mm^2 surface, obtaining an initial activity of 5μCi. The crystal has the [001] axis perpendicular to the 10×10-mm^2 face. To remove any radiation damage and to check the substitutional degree of the probes at cationic sites as a function of the annealing temperature, after the implantation the sample was annealed in air 30 min at 673 K, 30 min at 873 K, and 30 min at 1073 K, performing TDPAC measurements after each thermal treatment.

The measurements were recorded at RT in air and for a suitable set of crystal orientations using a coplanar arrangement of four BaF$_2$ detectors at 90° geometry, with a fast-fast coincidence logic and a resolution of 0.7 ns [55]. The sample was centered between detectors and oriented according to two different configurations, with its [001] crystalline axis normal to the detector plane ("lying sample"), and with its [001] axis parallel to the detector plane ("standing sample"), varying the "rotation" angle φ, as shown in Fig. 1. For both configurations, the TDPAC measurements were performed at $\varphi = 0°$, 10°, 20°, 30°, 40°, and 45°.

C. TDPAC results

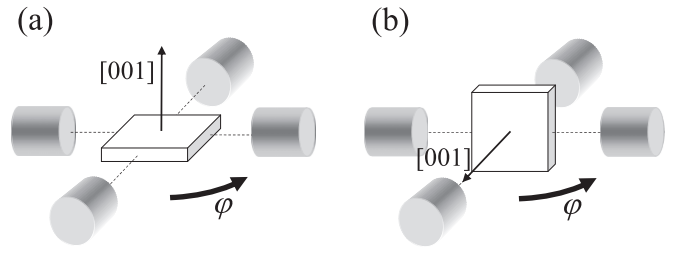The $R(t)$ spectra measured at RT for the complete set of the sample orientations described above are shown in Fig. 2.

FIG. 1. Single-crystal orientations in TDPAC measurements: (a) lying sample and (b) standing sample. In both configurations φ is rotation angle of sample around imaginary axis (not drawn) perpendicular to detector plane passing through center of sample. Both pictures correspond to $\varphi = 0°$. Arrow indicates orientation of [001] axis of hexagonal α-Al$_2$O$_3$ unit cell with respect to single crystal.

Here, the red solid lines are the best least-squares fits of Eq. (3) (letting the S_{2n} coefficients free in the fitting procedure as described in the previous section) to the $R(t)$ spectra (on the left) and, on the right are the Fourier transformations of the $R(t)$ fits. In the Fourier spectra we can identify the S_{2n}^{free} coefficients, which are related to the relative heights of the peaks present, as shown in the last spectra of Fig. 2.

Inspecting Fig. 2(a) [lying sample configuration, see Fig. 1(a)], the $R(t)$ spectra are similar for all orientations of the single crystal, i.e., it does not depend on the φ rotation angle. This behavior suggests that the charge distribution is axially symmetric (η close to zero) and that the V_{33} orientation is very close to a direction perpendicular to the detector's plane. In addition, inspecting Fig. 2(b) [standing sample configuration, see Fig. 1(b)], the S_{20}^{free} and S_{22}^{free} coefficients are those that have the stronger dependence on φ (S_{20}^{free} diminishes while S_{22}^{free} increases when φ increases), suggesting now that V_{33} rotates practically parallel to the detector's plane as φ varies. This hypothesis will be demonstrated when the calculated S_{Kn}^{eff} coefficients are discussed in Fig. 3.

It should be noted that if we fit Eq. (3) to the $R(t)$ spectra of Fig. 2(a), corresponding to the lying sample, with the hyperfine parameters of the unique HFI1 reported by Rentería *et al.* [44] before to anneal the sample at 1173 K [remember that after this annealing a second unexpected nonaxially symmetric polycrystalline HFI2 appeared, "breaking" the $R(t)$ spectra], the fit becomes satisfactory and it is not necessary to propose a second HFI to reproduce the experimental spectra. Nevertheless, if we fit the $R(t)$ spectra of Fig. 2(b), corresponding to the standing sample, with a unique HFI, the agreement is very bad (especially for $t > 25$ ns), showing the necessity to use more HFIs to reproduce the experimental spectra. It is worth noting here that the hyperfine parameters fitted for both experimental sample configurations and for every sample orientation with respect to the detectors must be the same, although the $R(t)$ spectra change due to the variation of the relative weights of the S_{2n}^{free} coefficients.

Hence, to correctly account for the whole set of the $R(t)$ spectra, two hyperfine interactions, HFIa and HFIb, were necessary. In Table I we show the parameters that characterize each HFI observed. Although these two HFIs are characterized by similar parameters, we can identify a fraction of ^{181}Ta
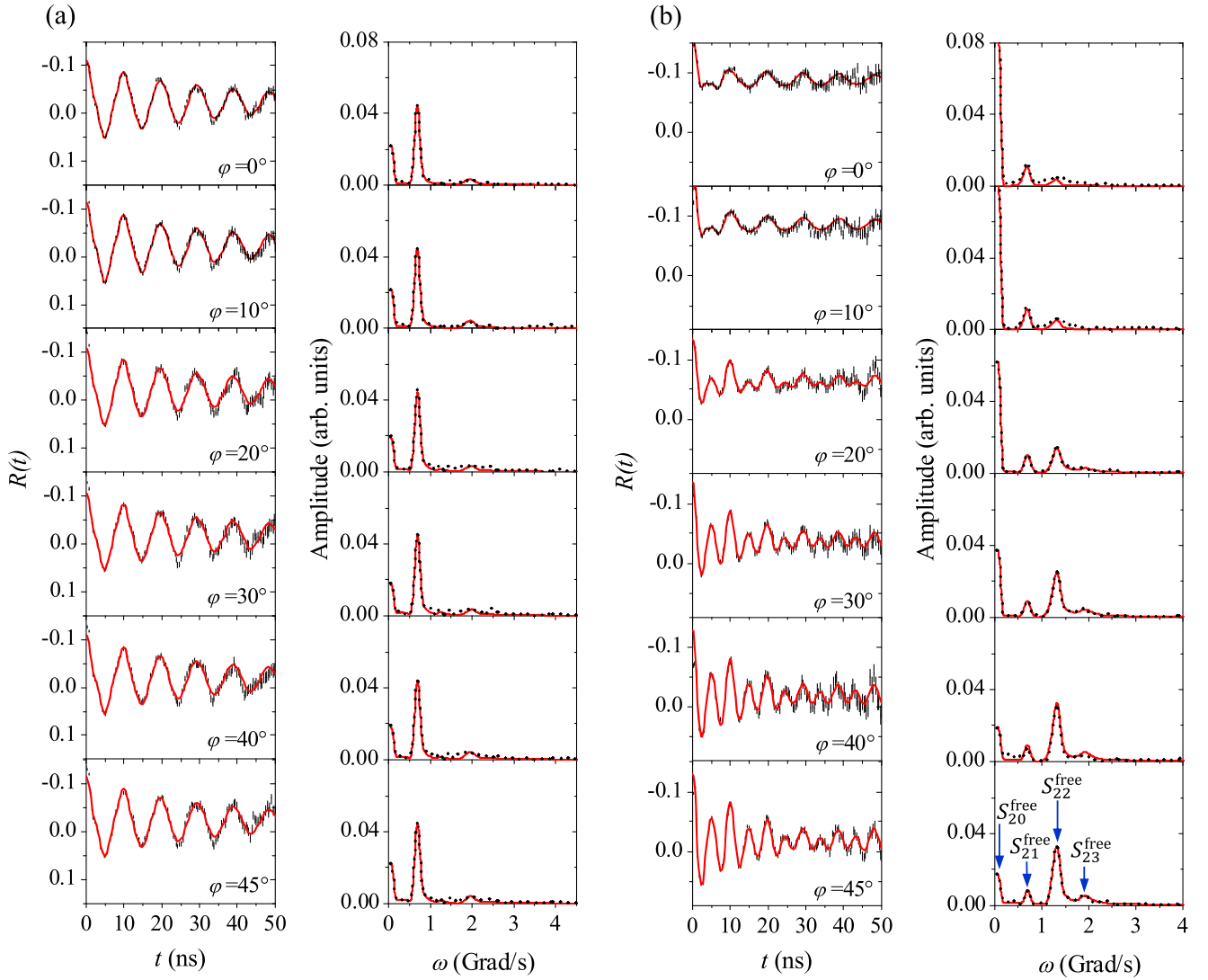
FIG. 2. $R(t)$ spectra (right) and their corresponding Fourier-transformed spectra (left) taken at room temperature for (a) lying sample and (b) standing sample configurations described in Fig. 1.

probes that senses the expected axially symmetric HFI (i.e., $\eta = 0$) and with its V_{33} parallel to the [001] crystal axis. The necessity to obtain precise and clean measurements for the standing sample configuration was a key fact to identify the existence of this axially symmetric HFI. If we compare the results reported in Table I with those reported by Rentería *et al.*, we see that HFI1 has the same parameters as the majority interaction (HFIa) reported here. When we fit the $R(t)$ spectra of Fig. 3(a) (lying sample, before the spectrum break) reported by Rentería *et al.* with two HFIs, we obtain the HFI parameters of HFIa and HFIb shown in Table I.

To obtain the orientation of the EFGs for each HFI with respect to the coordinate system formed by the detectors, we compare the experimental S_{2n}^{free} for the lying and standing sample configurations, and the calculated $S_{Kn}^{\text{eff}}(\eta)$ coefficients for different orientations of the EFG with respect to the detector's system, as described in Ref. [39]. Figure 3 shows the best agreement between the measured S_{2n}^{free}, for both interactions and the two sample configurations,

and their respective predicted $S_{Kn}^{\text{eff}}(\eta)$. Taking into account the hyperfine parameters shown in Table I, the $S_{Kn}^{\text{eff}}(\eta)$ were calculated with $\eta = 0.15$ and $\eta = 0$ for HFIa and HFIb, respectively.

First, the excellent agreement shown in Fig. 3 demonstrates that in this experiment both hyperfine interactions HFIa and HFIb correspond to probes localized in a *single-crystalline* atomic sites, with the V_{33} direction parallel to the [001] crystal axis, and with V_{22} and V_{11} directions parallel to the edges of the sample. Second, the quality of the spectra together with the strong variation of S_{K0}^{eff} and S_{K2}^{eff} for the standing configuration enabled the detection of HFIb, since in this configuration both coefficients are very sensitive to the small difference of the (low) η parameters of both interactions.

A rough inspection of Table I suggests that the hyperfine parameters that characterized HFIb are compatible with ^{181}Ta probes localized at the axially symmetric Al site free of defects. In Sec. IV we will discuss the nature of HFIa, after analyzing the assignment of HFIb enlightened by the complete *ab initio* study presented in the next section.
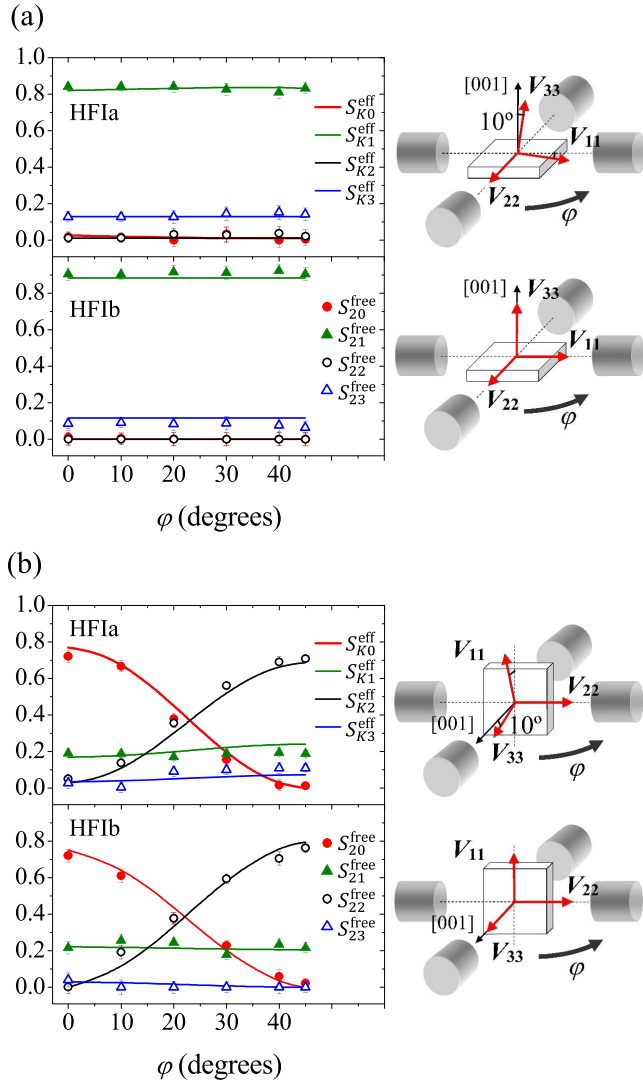
(a)

(b)

FIG. 3. Comparison between S_{2n}^{free} coefficients of HFIa (top) and HFIb (bottom) and their calculated $S_{Kn}^{\text{eff}}(\eta)$ ones for (a) lying sample and (b) standing sample configurations. In each case, on right, relative orientation of corresponding EFG tensor with respect to detectors is shown.

III. *AB INITIO* CALCULATIONS

A. Calculation details

All-electron *ab initio* calculations of the electronic structure in Ta-doped α-Al$_2$O$_3$ were performed within the DFT formalism to determine the equilibrium atomic structures

from the accurate description of the electronic density $\rho(\mathbf{r})$. The calculations were performed using the FP-APW+lo method [22] implemented in the WIEN2K code [57]. In addition, to check the correct inclusion of the U parameter we performed calculations using the PAW method [45,46], implemented in the Vienna *Ab initio* Simulation Package (VASP) code [45,58–61].

In WIEN2K, the wave functions are expanded into spherical harmonics inside nonoverlapping muffin-tin (MT) spheres of radius R_{MT} centered at the atoms, and in plane waves in the interstitial spaces. For this study we use $R_{\text{MT}}(\text{Al}) = 0.87$ Å, $R_{\text{MT}}(\text{Ta}) = 1.06$ Å, and $R_{\text{MT}}(\text{O}) = 0.85$ Å, and a cutoff parameter of the plane-waves bases of $R_{\text{MT}}K_{\text{max}} = 7$ (R_{MT} is the smallest radius used and K_{max} is the greatest modulus of the lattice vector in the reciprocal space). The tetrahedron method [46] was employed to integrate in the reciprocal space, and a k-space grid of $5 \times 5 \times 3$ was selected for the $2 \times 2 \times 1$ SC. Exchange and correlation effects were treated using the Perdew-Burke-Ernzerhof parametrization of the generalized-gradient approximation (PBE-GGA) [62]. The equilibrium atomic positions were obtained relaxing the structures until the forces on all ions were lower than 0.01 eV/Å, and the EFG tensor was calculated from the second derivative of the full potential [63,64] of these equilibrium structures.

To perform VASP calculations, we selected the PAW-PBE potentials according to the valence configuration Ta ($5p^6\,6s^2\,5d^3$), Al ($3s^2\,3p^1$), and O ($2s^2\,2p^4$). In the case of the plane-wave basis expansion, a cutoff energy of 400 eV was selected for all the calculations. Like in WIEN2K, the k-space grid was adjusted for each dilution, taken in the case of $2 \times 2 \times 1$ SC a $5 \times 5 \times 3$ grid, which ensures convergence in terms of forces and total energy, and also the structures were optimized until the forces in all the atoms were lower than 0.01 eV/Å.

For a better description of the electronic localization of Ta-d states, a Hubbard correction implemented in the DFT+U methodology was applied, according to the Dudarev approximation [65] as implemented in VASP, which utilized a $U_{\text{eff}} = U - J$ single parameter (with U and J the Coulomb and exchange parameters, respectively). In order to select a proper U_{eff} value for describing the studied system we adopted the linear response approach described by Cococcioni *et al.* [66], for VASP, and the general procedure described by Madsen and Novák [67] for WIEN2K. With this, we found that $U_{\text{eff}} = 3.2$ eV is sufficient for describing the localization of the Ta-d states.

Crystalline α-Al$_2$O$_3$ primitive unit cell is rhombohedral [see Fig. 4(a)], belonging to $R\bar{3}c$ space group containing 4

TABLE I. Experimental parameters that characterize both hyperfine interactions observed. To obtain V_{33} from ω_Q we used Q ($I = +5/2$) = $+2.35(6)$ barn of the 482 keV nuclear state of ^{181}Ta [56]. Error in V_{33} does not consider propagation error of Q. ω_Q and hence V_{33} signs are not determined in the experiment.

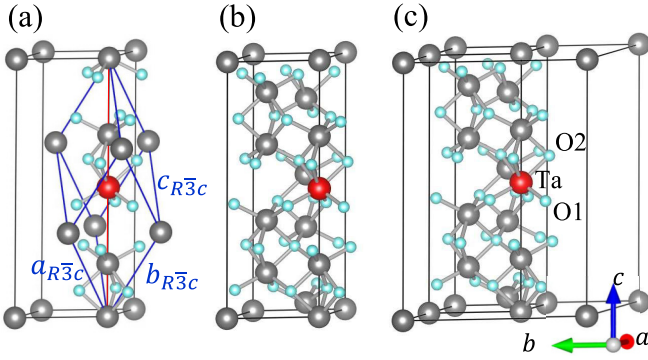|	ω_Q (Mrad/s)	η	V_{33} (10^{21} V/m^2)	V_{33} direction	δ (%)	f (%)
HFIa	102.4(9)	0.14(5)	11.4(1)	[001]$-10°$ [a]	5.1(8)	77(8)
HFIb	108.9(9)	0.03(3)	12.1(1)	[001] [b]	0.0(7)	23(4)

[a] 10° uncertainty.
[b] 2° uncertainty.

FIG. 4. Crystalline α-Al_2O_3 unit cell in (a) rhombohedral and (b), (c) hexagonal representations. Gray and light-blue balls represent Al and O atoms, respectively. (c) Size of $2 \times 2 \times 1$ SC with only one Ta (red) impurity substituting Al atom in center of SC.

Al and 6 O atoms; nevertheless, usually it is referred in a hexagonal representation that contains three primitive cells [i.e., 12 Al and 18 O atoms, as shown in Fig. 4(b)] with $a = b = 4.75999(3)$ Å and $c = 12.99481(7)$ Å [68]. The Al atoms occupy $\pm(0, 0, u)$; $\pm(0, 0, u + 1/2)$; *rh* positions, and the O atoms occupy $\pm(v, 0, 1/4)$; $\pm(0, v, 1/4)$; $\pm(-v, -v, 1/4)$; *rh*, where *rh* implies to translate $(1/3, 2/3, 2/3)$ and $(2/3, 1/3, 1/3)$ to the precedent positions, with $u = 0.35219(1)$ and $v = 0.30633(5)$ [68].

To model the doped systems, we use an α-Al_2O_3 SC in which an Al atom is replaced by a Ta one, as shown in Fig. 4. We call this system Al_2O_3:Ta^0. Considering the double-donor nominal character of Ta^{5+} when it replaces Al^{3+} in α-Al_2O_3, we need to model the possible ionization of these 2 donor electrons, a process that can occur under the present experimental conditions. In this sense we performed calculations removing 1 and 2 electrons from the Al_2O_3:Ta^0 system, calling them Al_2O_3:Ta^{1+} and Al_2O_3:Ta^{2+}, respectively. To correctly model the experimental impurity dilution (i.e., an isolated impurity), the calculations were performed in large SCs to guarantee the total convergence of the hyperfine parameters, as a function of the SC size, when a native Al atom is replaced by a Ta (impurity) one. Particularly, we study the convergence of the EFG tensor because it is extremely sensitive to small changes in the charge density surrounding the probe nucleus due to its r^{-3} dependence from their charge sources. For this study, we performed calculations in the primitive rhombohedral cell (Rh), the hexagonal cell (Hx), and SCs containing 4 ($2 \times 2 \times 1$), 9 ($3 \times 3 \times 1$), and 32 ($4 \times 4 \times 2$) hexagonal unit cells, obtaining 1:4, 1:12, 1:48, 1:108, and 1:384 impurity cation dilution, respectively. As we showed in Ref. [69], it is essential to study the impurity dilution for all the charge states considered.

It is well known that the FP-APW+lo method describes very accurately the electronic charge density in the close neighborhood of the atomic nucleus, providing in this way a correct prediction of the EFG tensor. The comparison between the EFG and the electronic structure predicted by this method and those using the VASP code for increasing dilutions up to the $3 \times 3 \times 1$ SC shows an excellent agreement. In this sense, to study the impurity dilution, and since VASP requires fewer

computing capabilities than WIEN2K, we employed VASP to perform the complete study in very large SCs.

Finally, there is no experimental evidence of magnetic dipole interactions at ^{181}Ta sites in ^{181}Ta-doped α-Al_2O_3 semiconductor; nevertheless, since in this case the Ta impurity could leave unpaired electrons leading to a net magnetic moment in the SC, non-spin-polarized (NSP) and spin-polarized (SP) *ab initio* calculations were performed. For both calculations the optimized U_{eff} parameter agrees within 0.1 eV.

To calculate the defect-formation energy, we follow the formalism presented in Ref. [70], where (considering an O-rich environment of the impurity) it is given by

$$\begin{aligned} E_f(Al_2O_3 : Ta)^q = {} & E(Al_2O_3 : Ta)^q - E(Al_2O_3) + \mu_{Al}^* \\ & + \tfrac{1}{2}\, \Delta_f H^{Al_2O_3} - \mu_{Ta}^* - \tfrac{1}{2}\, \Delta_f H^{Ta_2O_5} \\ & + q(\varepsilon_F + \varepsilon_v') \end{aligned} \quad (6)$$

where $\Delta_f H$ are the oxide formation enthalpies and μ^* the total energy per atom of the corresponding metallic crystal. The Fermi energy ε_F ($0 \leqslant \varepsilon_F \leqslant \varepsilon_g$, ε_g is the band-gap energy) is referred to the top of the valence-band (TVB) energy ε_v' ($\varepsilon_v' = \varepsilon_v + \delta_q$), where ε_v is the TVB energy of the pure system and δ_q lines up the band structures of the system with and without impurity (pure system).

One important thing to remark is that we did not use total energies from non-neutral calculations performed with VASP, due to its limitations to describe charged systems, particularly at the Ta dilutions presented in this work. For this reason, the defect-formation energies were calculated in an accurate way with the WIEN2K code, as we already performed successfully in Refs. [69–71].

B. Calculation results and discussion

1. Impurity dilution

First, we determined the size of the Ta-doped SC suitable to simulate the *isolated Ta impurity condition*, i.e., the smallest SC where each impurity does not interact with another one, and its neighbors can relax freely without being affected by the relaxations of the neighbors of the closest impurities. For this, we studied the convergence of the EFG tensor as a function of the Ta impurity dilution, increasing the size of the SC for the three charge states studied. We found that a $2 \times 2 \times 1$ SC (1:48 impurity cation dilution) is necessary to simulate the isolated impurity condition for all the Ta-doped α-Al_2O_3 systems studied here. For clarity, in Fig. 5 we show the predicted value of V_{33} as a function of the number of cations in the SC (i.e., as a function of the size of the SC) for only Al_2O_3:Ta^0 and Al_2O_3:Ta^{2+} with and without the $U = 3.2$ eV parameter. In effect, for $2 \times 2 \times 1$ SC all the V_{33} calculations are converged. The same convergency condition was found for the same SC size when spin-polarized calculations were used. The arrows on the right of Fig. 5, corresponding to WIEN2K predictions of V_{33} for the $2 \times 2 \times 1$ SC, slightly differ from the VASP values due to the slightly different atomic equilibrium positions predicted by both methods. When using the same positions, both methods predict basically the same EFG tensor, as deeply discussed in Ref. [72].

From now on, all *ab initio* results shown and discussed will be those of the $2 \times 2 \times 1$ SC. It is interesting to note
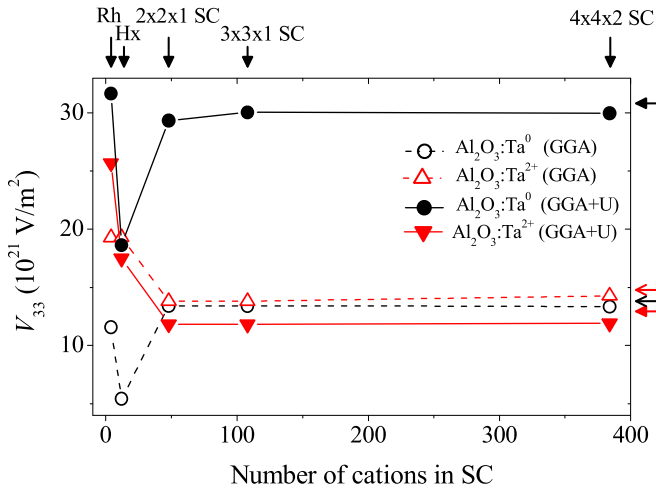
FIG. 5. Calculated V_{33} using VASP as function of number of cations in SC for Al_2O_3:Ta^0 (black) and Al_2O_3:Ta^{2+} (red) systems. Open and filled symbols correspond to GGA and GGA + U predictions, respectively. Arrows at top show sizes of cells and SC employed in calculations. From left to right their corresponding dilutions are 1:4, 1:12, 1:48, 1:108, and 1:384, respectively. Open and filled arrows on right indicate WIEN2K predictions for $2 \times 2 \times 1$ SC for GGA and GGA + U, respectively.

FIG. 6. Defect-formation energy E_f (solid lines) as function of Fermi-energy level ε_F for Al_2O_3:Ta^q ($q = 0$, 1+, and 2+). ε_g is predicted band gap of pure α-Al_2O_3 system. Dashed lines correspond to spin-polarized calculations. For Al_2O_3:Ta^{2+} both lines are indistinguishable.

that if the impurity probe atom in α-Al_2O_3 is Cd instead of Ta, the condition of isolated impurity is found using the Hx supercell [70], a dilution (1:12 impurity cation dilution) four times lower than that needed for Ta to achieve this condition.

2. EFG, impurity's formation energy analysis, and charge states

As a first step, we performed EFG calculations at Ta sites in Ta-doped α-Al_2O_3 as a function of the charge state of the $2 \times 2 \times 1$ SC using the PBE-GGA approximation. In the first two columns of Table II, we show the V_{33} predictions calculated for the Al_2O_3:Ta^0, Al_2O_3:Ta^{1+}, and Al_2O_3:Ta^{2+} systems, after the full structural atomic relaxation. For all the charge states, as expected from the structural symmetry at the cation site, the predicted asymmetry parameter is null and the V_{33} direction is parallel to the [001] axis. First, guided by the absence of magnetic hyperfine interactions in the experiments, we performed the NSP calculations (Table II, first column), finding that the neutral (Al_2O_3:Ta^0) SC was the can-

TABLE II. V_{33} predicted for equilibrium structures using GGA and GGA + U for $Al_2O_3 : Ta^q$ ($q = 0$, 1+, and 2+) systems, applying NSP and SP calculations. Experimental V_{33} is the value determined for HFIb (see Table I).

	V_{33} (10^{21} V/m^2)			
	GGA		GGA + U	
	NSP	SP	NSP	SP
Al_2O_3:Ta^0	+13.29	+32.89	+30.84	+31.20
Al_2O_3: Ta^{1+}	+22.03	+24.29	+24.01	+25.15
Al_2O_3:Ta^{2+}	+14.78	+15.12	+12.95	+12.99
Exp.	12.1(1)			

didate to represent the physical situation as the origin of HFIb, being the closer prediction to the experimental V_{33} value. On the other hand, the SP calculations showed a very different situation (second column): we found that the spin-polarized solutions for Al_2O_3:Ta^0 and Al_2O_3: Ta^{1+} are the energetically most stable with respect to the NSP ones, predicting a magnetic solution for these charge states. Contrary, for the Al_2O_3:Ta^{2+} system we did not find a magnetic solution. These results enable in principle to discard Al_2O_3:Ta^0 as responsible for HFIb since the predicted V_{33} (+32.89 × 10^{21} V/m^2) is in clear disagreement with the experimental value and would imply the presence of a combined electric-quadrupole plus dipole-magnetic interaction. The same considerations apply to the Al_2O_3: Ta^{1+} system in which the predicted V_{33} is also far away from the experimental value. To totally demonstrate that Al_2O_3:Ta^{2+} is now the candidate originating HFIb, defect-formation energy calculations were performed. In Fig. 6 the system with lower defect-formation energy is Al_2O_3:Ta^{2+}, i.e., when 2 electrons are removed from the SC. As shown in this figure the conclusion is the same for both NSP and SP calculations.

However, the predicted V_{33} value for Al_2O_3:Ta^{2+} is 25% higher than the experimental one, which was determined with 1% uncertainty due to the highly local sensitivity of the TDPAC technique. Since it is crucial to describe with high precision the electronic density near the Ta probe atom, particularly for the accurate calculation of the EFG, we performed electronic structure calculations taking into account the strong correlation between the Ta-5d states through the inclusion of the Hubbard onsite U parameter for these Ta orbitals. As we will show later in Sec. III B 4, both the Ta-d and Ta-p contributions to the EFG will be the relevant ones. Although U is only applied to the Ta-d states, Ta-p states also resulted in being affected, a fact that will be crucial at the origin of the EFG.

First, using the GGA + U approximation we obtained that the overall shape of the defect-formation energy plot of Fig. 6
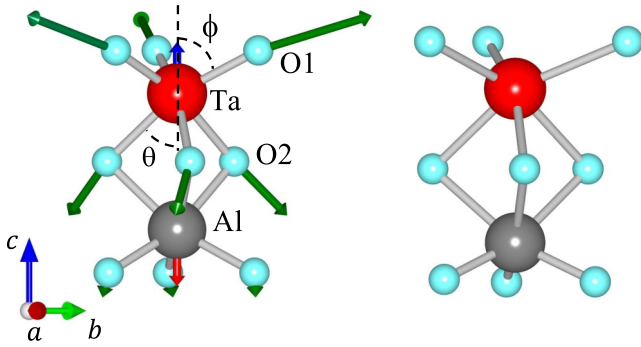
FIG. 7. Local coordination of substitutional Ta impurity in α-Al$_2$O$_3$ structure. On left, unrelaxed structure showing atomic displacements of Ta (red), oxygen (light-blue), and Al (gray) atoms. On right, final relaxed structure for Al$_2$O$_3$:Ta^0 ($2 \times 2 \times 1$ SC), magnifying atomic displacement by factor of 3.

does not change, confirming that the Al$_2$O$_3$:Ta^{2+} system has the lower formation energy. The defect-formation energy predictions using GGA + U decreases in less than 0.1 eV with respect to those calculated using GGA since the onsite U parameter only affected a certain type of orbitals of *only one* atom in the $2 \times 2 \times 1$ SC that contains 120 atoms.

On the other hand, the inclusion of the U parameter was revealed essential for the correct description of the EFG. In effect, the last two columns in Table II show the GGA + U predictions for V_{33}. In this case also, the predicted asymmetry parameter is null and the V_{33} direction is parallel to the [001] axis. Again, the SP calculations for Al$_2$O$_3$:Ta^0 and Al$_2$O$_3$: Ta^{1+} give magnetic solutions, and nonmagnetic for Al$_2$O$_3$:Ta^{2+}. The inclusion of the U parameter changes strongly V_{33} in the case of the NSP neutral SC (Al$_2$O$_3$:Ta^0), extremely far from the experimental value, and moves to a less extent the V_{33} prediction of the double-ionized Al$_2$O$_3$:Ta^{2+} SC, for both NSP and SP calculations. For this charge state, the NSP solution has the lower energy and the predicted EFG agrees perfectly well with the experimental value of the pure electric-quadrupole interaction HFIb.

After considering the defect-formation energy study and both the experimental and *ab initio* results for the EFG at the ^{181}Ta site, we can see that the inclusion of the U parameter for Ta-5d orbitals is necessary to correctly describe the electronic structure in the neighborhood to the Ta probe atom in Ta-doped α-Al$_2$O$_3$ semiconductor.

In order to show and interpret the effects produced on the electronic density by the inclusion of the U parameter and the differences produced in the EFG predictions, we next analyzed the structural relaxations and the electronic structure of the studied doped systems using GGA and GGA+U.

3. Structural relaxations

When a Ta impurity replaces an indigenous Al atom in the corundum Al$_2$O$_3$ lattice it produces forces in all the atoms of the SC being not negligible on the impurity's nearest-neighbor atoms. This effect produces atomic structural relaxations proportional to these forces. Figure 7 shows the sixfold coordination of the Ta impurity with their 3 O1 and 3 O2 nearest oxygen atoms. These O2 atoms coordinate with a nearest Al atom, forming a unit composed of 4 tetrahedra with open space along the c axis and below and above this unit. The arrows on the unrelaxed structure (on the left) show the directions and relative magnitudes of the atomic displacements, which decrease strongly with the distance from the Ta atom. The O1 atoms move essentially within the a-b plane while the O2 atoms move more along the c axis. The Ta and Al atoms move away along the c axis, in opposite directions towards the open space. On the right, the final atomic positions are shown after multiplying the displacements by 3 for the Al$_2$O$_3$:Ta^0 system. The qualitative behavior of the structural relaxations is the same for all the charge states studied, as shown in Table III. This table shows experimental Al-O1 and Al-O2 distances, and ϕ and θ angles that these bonds form with the c axis, respectively, in pure (undoped) α-Al$_2$O$_3$ structure. These values are compared with the results for Ta-O1 and Ta-O2 bonds obtained using GGA and GGA + U for Al$_2$O$_3$:Ta^0, Al$_2$O$_3$:Ta^{1+}, and Al$_2$O$_3$:Ta^{2+} systems. These results do not change for SP calculations. As shown in Fig. 7, Ta produces anisotropic outward relaxations for the inequivalent O1 and O2 nearest neighbors, relaxations

TABLE III. M-O1 and M-O2 distances, and ϕ and θ angles that these bonds form with c axis (see Fig. 7), respectively, in pure (undoped) α-Al$_2$O$_3$ structure (M = Al) and Ta-doped Al$_2$O$_3$ (M = Ta), using GGA and GGA + U for Al$_2$O$_3$:Ta^q ($q = 0, 1+, 2+$) systems for $2 \times 2 \times 1$ SCs.

	α-Al$_2$O$_3$			
	d(Al-O1) (Å)	d(Al-O2) (Å)	ϕ (°)	θ (°)
Exp.[a]	1.854	1.972	63.14	47.67

	α-Al$_2$O$_3$:Ta							
	GGA				GGA + U			
	d(Ta-O1) (Å)	d(Ta-O2) (Å)	ϕ (°)	θ (°)	d(Ta-O1) (Å)	d(Ta-O2) (Å)	ϕ (°)	θ (°)
Al$_2$O$_3$:Ta^0	2.034	2.117	65.07	46.67	2.035	2.112	65.24	45.97
Al$_2$O$_3$: Ta^{1+}	1.975	2.076	64.73	46.64	1.974	2.077	64.96	46.48
Al$_2$O$_3$:Ta^{2+}	1.909	2.041	64.67	46.92	1.910	2.039	64.35	47.08

[a]Reference [68].
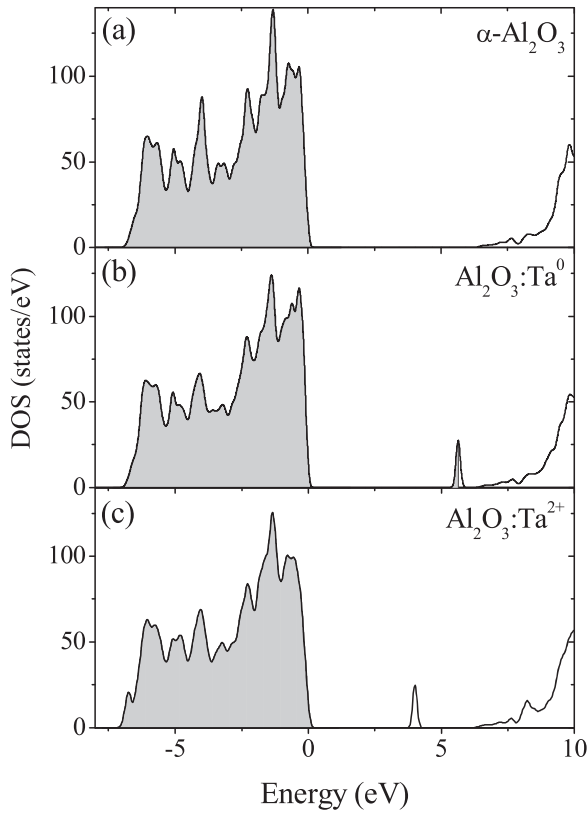
FIG. 8. Total density of electronic states (DOS) of (a) pure α-Al$_2$O$_3$, (b) Ta-doped Al$_2$O$_3$:Ta^0, and (c) Ta-doped Al$_2$O$_3$:Ta^{2+}, using GGA. Zero energy refers to top of valence band. Shaded areas are occupied states. In (b), Fermi level is at middle of donor impurity level, and in (c) at top of valence band.

that decrease with the ionization of the impurity level, related to a decreasing Coulombic repulsion effect. The use of the DFT $+ U$ formalism does not introduce significant structural

changes with respect to DFT, evidencing that the differences in the EFG predictions between both formalisms come from the modification of the electronic structure description, unraveling both structural and electronic effects.

4. Electronic structure and the EFG

In this section, the modification introduced using the DFT $+ U$ formalism on the electronic structure of the doped systems and its relation with the EFG produced by the resulting electron density are presented and discussed.

Figure 8 shows the total density of electronic states (DOS) of pure α-Al$_2$O$_3$, Al$_2$O$_3$:Ta^0, and Al$_2$O$_3$:Ta^{2+} using GGA. The Ta atom introduces a very energy-localized impurity level in the band gap close to the bottom of the conduction band. The shaded areas represent occupied states, corresponding to 2 electrons in the occupied states at the impurity level [Fig. 8(b)]. When electronic charge is removed from the SC, the Fermi level moves to lower energies inside the impurity level (and the peak itself moves to the left), lowering the energy of the system. If 2 electrons are removed, the Fermi level results localized at the TVB and the impurity level becomes completely empty [Fig. 8(c)]. The inclusion of the U parameter does not affect the general shape of the total DOS in the valence band. This can be understood since in this study the U parameter is applied to the d states of only 1 Ta atom in the 120-atom SC. Nevertheless, a closer inspection of d- and p orbitals at the valence band and at the impurity level in the partial DOS (PDOS) shows interesting changes that reflect modifications in the electronic density close to the Ta nucleus when U is applied that will affect the EFG behavior, as shown in Table II.

Figures 9 and 10 show Ta-d and Ta-p PDOS, respectively, using GGA and GGA $+ U$ for NSP and SP calculations. Let us discuss first the strong change in V_{33} for the Al$_2$O$_3$:Ta^0 when U is added in the NSP calculations. Ta-d_{z^2} and Ta-p_z orbitals at the impurity level [Figs. 9(a) and 10(a), respectively],
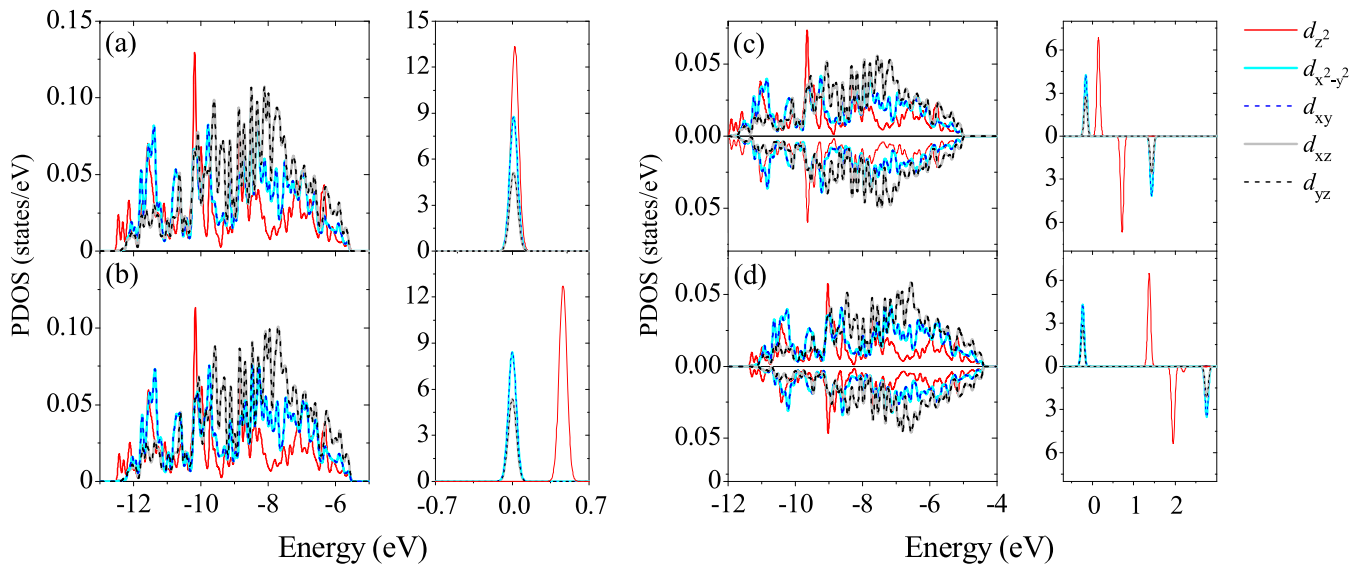

FIG. 9. Ta-d partial density of electronic states (PDOS) of Al$_2$O$_3$:Ta^0 system for (a) GGA and (b) GGA $+ U$ non-spin-polarized (NSP) results; (c) GGA and (d) GGA $+ U$ spin-polarized (SP) results. In each figure valence band is shown in left panel and impurity level is zoomed in right panel. Zero energy refers to Fermi level. Z axis of the local coordinate system used in the calculations at the Ta site is parallel to the [001] crystalline axis.
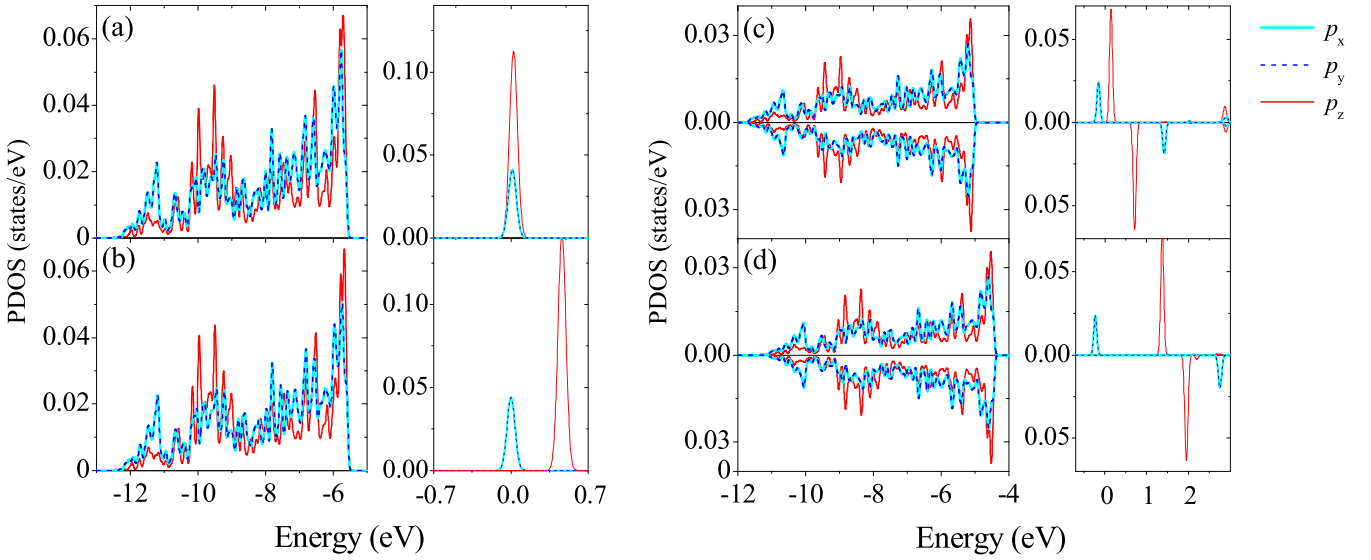
FIG. 10. Ta-p PDOS of Al_2O_3:Ta^0 system for (a) GGA and (b) GGA $+ U$ NSP results; (c) GGA and (d) GGA $+ U$ SP results. In each figure valence band is shown in left panel and the impurity level is zoomed on right panel. Zero energy refers to Fermi level. Z axis of the local coordinate system used in the calculations at the Ta site is parallel to the [001] crystalline axis.

which contributes with negative charge localized along the [001] crystal axis ($\equiv z$) and therefore to a negative V_{33} value [70], moves to the right with respect to the Fermi level when the U parameter is added [see Figs. 9(b) and 10(b), respectively], emptying these states, producing a very positive V_{33} final value ($+30.84 \times 10^{21}$ V/m^2), as shown in the first row of Table II. All this behavior of V_{33} can be understood inspecting the equations for the p and d asymmetry counts Δn_p and Δn_d, which are proportional to the EFG contributions V_{33}^p and V_{33}^d (see Eqs. (4) and (5) in Ref. [70]). A close inspection of Table IV, which shows p and d contributions to the EFG, indicates that the large increase in V_{33} is basically due to the d contribution, in agreement with the relative weight in two orders of magnitude of these states over the p ones at the impurity level. In Fig. 9 the relative weight of the impurity d states is very large compared to the valence-band d states, which in addition do not change when U is added. In turn, in Fig. 10 the impurity- and valence-band p states have the same weight and will have an opposite behavior between them relative to the EFG. In effect, when U is added, a small decrease of V_{33}^p is observed (see Table IV, first row). This is due to an opposite behavior of the p_z states in the valence band (in which the negative p_z contribution increases, decreasing V_{33}^p) and those at the impurity level (in which the p_z contribution

decreases to a less extent). On the other hand, when negative charge is removed from the SC and hence the impurity level is totally emptied (essentially, emptying the majority d states), the V_{33}^p contribution dominates over the V_{33}^d one, as shown in Table IV (last row).

The strong localization in energy of the impurity level shown in the DOS is correlated with a high spatial localization of its electron charge density $\rho(\mathbf{r})$, as shown in Figs. 11 and 12. The electron density $\rho(\mathbf{r})$ shown in each figure corresponds to the 2 donor electrons that can be ionized in the real sample under the experimental conditions. This electronic charge is essentially of Ta-d character, in agreement with the relative weights shown in the PDOS by the d and p contributions at the impurity level. Figure 11 shows $\rho(\mathbf{r})$ at planes (001) containing (a) the 3 O1 atoms, (b) the Ta atom, and (c) the O2 atoms. The green triangular spot in Fig. 11(a) shows more evidently than in Fig. 11(c) the antibonding behavior of the d states, which are strongly localized in the GGA calculation and even more when U is added. In Fig. 11(b), the electronic charge is distributed following also an antibonding behavior: the green cloud with respect to the O1 atoms and the yellow one with respect to the O2 atoms.

To understand the V_{33} behavior when U is added and also when negative charge is removed from the SC, Fig. 12 is more suited. In Fig. 12(a) one O1 and one O2 atoms are present together with the Ta atom. The electronic charge is antibonding distributed, localizing as far as possible from the Ta-O1 and Ta-O2 bonds. When U is added this effect is much more pronounced (electronic charge disappeared from the [001] $\equiv$ c crystalline axis). The same antibonding behavior can be seen in Fig. 12(b) in which O1 and O2 are not contained at the plane but are equidistant from it. The redistribution of negative charge, clearly seen in Fig. 12(a), is responsible for the strong increase of the positive V_{33} value (from $+13.29$ to $+30.84 \times 10^{21}$ V/m^2; see Table II) for Al_2O_3:Ta^0. The angle

TABLE IV. p and d contributions to V_{33} using GGA and GGA $+ U$ NSP calculations as function of charge state of $2 \times 2 \times 1$ SC.

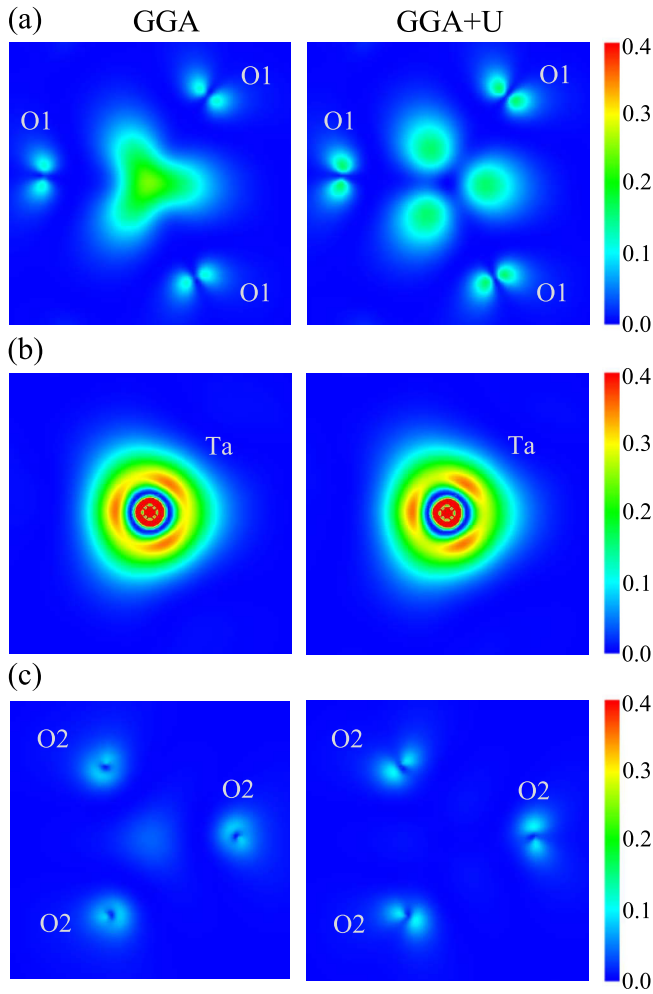|	V_{33}^p (10^{21} V/m^2)		V_{33}^d (10^{21} V/m^2)	
	GGA	GGA $+ U$	GGA	GGA $+ U$
Al_2O_3:Ta^0	$+8.34$	$+7.78$	$+4.86$	$+23.36$
Al_2O_3: Ta^{1+}	$+10.16$	$+10.60$	$+11.44$	$+12.94$
Al_2O_3:Ta^{2+}	$+14.38$	$+13.34$	$+0.15$	$+0.10$

FIG. 11. Electron density $\rho(\mathbf{r})$ in Al_2O_3:Ta^0 system corresponding to energy range of occupied states at impurity level projected at (001) planes containing (a) O1 atoms, (b) the Ta atom, and (c) O2 atoms, using GGA (left) and GGA + U (right).
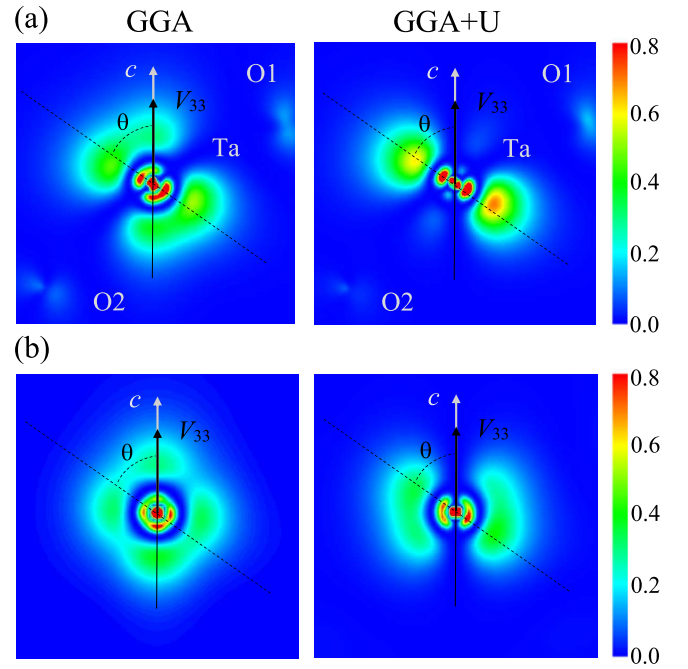

FIG. 12. Electron density $\rho(\mathbf{r})$ in Al_2O_3:Ta^0 system corresponding to energy range of occupied states at impurity level projected at (a) (010) plane containing O1, O2, and Ta; and (b) (110) plane containing only Ta atom, using GGA (left) and GGA + U (right). V_{33} direction coincides with [001] ($\equiv c$) crystalline axis. $\theta = 54.7°$ is angle that separates regions of negative charge contributing with positive or negative values to V_{33} (see text).

$\theta = 54.7°$ separates regions of negative charge contributing with opposite signs to V_{33} (see Eq. (14) of Ref. [71]): charge localized below θ (in fact, a conical region in three dimensions with V_{33} as its symmetry axis) contributes with negative values and vice versa. When U is added, negative charge disappears from the [001] (c) axis and in addition charge is localized for angles larger than θ (closer to the (001) plane), contributing with positive values to V_{33}. In Fig. 12(b) the charge redistribution when U is added goes in the same sense, increasing the positive V_{33} value. When 1 and 2 electrons are removed from this SC, essentially this charge is gradually removed from the clouds shown in Fig. 12, strongly decreasing V_{33} until the V_{33}^d contribution vanishes when the 2 donor electrons are removed (see Table IV). In this case, the total V_{33} comes from the p contribution, as mentioned before. The addition of U in this ionized state produces a relatively small change in V_{33}^p but is very relevant when compared with the experimental V_{33} value. This change is due to the few d states present at the valence band which are affected by the U parameter applied to the Ta-d states in Al_2O_3:Ta^{2+}, which in turn modify the p states of the valence band.

Now, if we take into account the spin polarization in the PDOS calculations, we see in Figs. 9(c) and 9(d) and 10(c) and 10(d) that Ta-d_{z^2} and Ta-p_z are empty already before adding the U parameter, being the other states of the impurity level (below the Fermi energy) *completely* filled by the 2 donor electrons, stabilizing the system, in agreement with the fact that the SP solution for Al_2O_3:Ta^0 is that of lower energy. In reference to these states located just below the Fermi level, there are degenerate states being contributed on one hand by Ta-d_{xz}/Ta-d_{yz} and on the other hand by Ta-d_{xy}/Ta-d_{x2-y2}. When U is added, these filled states move to the valence band, lowering the energy of the system, and the d_{z^2} and p_z empty states move to higher energies. Both electronic configurations (spin-polarized GGA and GGA + U) give the same high V_{33} value already discussed. When the 2 electrons are removed, both GGA and GGA + U SP solutions became nonmagnetic and, as mentioned before, the NSP solutions for Al_2O_3:Ta^{2+} have the lower energy. In both SP and NSP calculations the filled states of the valence band are basically the same, generating very similar EFGs.

IV. DISCUSSION

In Sec. II C, Table I resumed the parameters of the two hyperfine interactions observed in the present TDPAC experiments. Although both interactions have very similar

parameters, the small differences between them are important for their interpretation when they are compared with the *ab initio* calculations. HFIb could only be observed in the present experiments, since as already mentioned a clean measurement was needed with the sample positioned with the *standing configuration* [Fig. 2(b)]. HFIa is characterized by a nonzero low-asymmetry parameter and a more distributed V_{33}, both in magnitude and orientation, close to the values of HFIb. The correct assignment of these interactions would not have been possible without this complete *ab initio* electronic structure and defect-formation energy study, and without the precise measurement of HFIb. If only NSP calculations would have been considered (see Table II), taking into account that magnetic interactions were not observed in the experiment, an uncertain assignment of the interactions would result since two of these predictions agreed with the experimental EFG, being the closer prediction that of Al_2O_3:Ta^0. The SP calculations showed that for this charge state the solution is magnetic with an EFG in clear disagreement with the experiment and that Al_2O_3:Ta^{2+} is nonmagnetic with its EFG now the closer to the experiment (for this charge state, SP and NSP EFGs are coincident). The defect-formation energy study showed that Al_2O_3:Ta^{2+} is the one with lower energy, reinforcing its assignment to HFIb. Finally, the correct treatment of the Ta-5d states using the Hubbard U formalism leads to a better agreement with the experiment, giving the correct assignment for HFIb, i.e., this interaction is produced by doubly ionized ^{181}Ta probes localized at defect-free substitutional Al sites in α-Al_2O_3.

Regarding HFIa, it can be assigned to ^{181}Ta probes, also doubly ionized, but localized at Al sites with some degree of slight structural disorder in their distant neighborhood. In addition to the fact that the Al_2O_3:Ta^{2+} system is predicted as that with the lowest energy, it is important to mention that in our high-purity (99.99%) α-Al_2O_3 commercial single-crystalline samples both the presence of acceptor impurities (like K, Mg, Mn, Na, and Ni) even at trace levels (ppm for each of these impurities) and the experimental temperature effect promote the ionization of the 2 donor electrons to the conduction band and their diffusion and entrapment at these acceptor centers. We recall here that the donor electrons supplied by the Ta atoms are in parts per million concentrations in these doped samples, accordingly with the ^{181}Ta impurity dilution achieved by the ^{181}Hf ($\rightarrow$ ^{181}Ta) ion implantation process. In this sense the number of acceptor centers is extremely large with respect to the number of donor electrons to be ionized. It is interesting to mention at this point that the impurities mentioned above which are present in the real samples used in the experiments act as an acceptor "reservoir" of the Ta's donor electrons, whose Fermi energy must be relatively low (close to the TVB), this Fermi energy being the one to be used in Fig. 6, leading to Ta^{2+} as the most probable charge state (that with the lowest energy), moreover considering that the experimental temperature promotes the ionization.

It is worth noting that the clean and precise TDPAC experiment presented here, necessary to observe and characterize the nonmagnetic HFIb, gives the experimental value of the exact same physical situation that can be modeled by the *ab initio* calculations. Contrary, many configurations of the

defect neighborhood should be considered for HFIa, without experimental certainty of which is the real situation.

On the other hand, this complete comparison between such an experiment at the subnanoscopic level, defect-formation energy calculations, and accurate electronic structure study and EFG predictions from first principles, which was revealed essential to disentangle the hyperfine interaction assignments exposed in Table II, showed that it is necessary to introduce the U parameter to correctly describe the electronic localization of Ta-d states acting as a diluted impurity.

It is very interesting to note that in all previous combined experimental and theoretical studies performed by us using ^{181}Ta as diluted impurity probe in rutile TiO_2 and SnO_2 semiconductors [39,40], the inclusion of the Hubbard U parameter accounting for the Coulomb interaction of the Ta-5d states was not necessary to reproduce the experimentally observed EFGs. In both oxides, Ta is nominally a donor impurity, and it is revealed to introduce a *flat* impurity level at the bottom of the conduction band. The predicted EFGs for both ionized and nonionized states in each oxide are indistinguishable within the experimental error. In this sense, in both cases a controversy between the measured EFG and the predicted ones could not arise even in case a defect-formation energy analysis is added, as occurs in this work with Ta-doped Al_2O_3. Moreover, none of the reported *ab initio* calculations in the literature modeling oxides doped with the ^{181}Ta impurity probe used the U parameter to treat the Ta-5d states, because neither potential controversy was produced since a complete defect-formation energy study were not done.

To complete this study, now we calculated the EFG tensor using GGA + U for Ta-doped TiO_2 and Ta-doped SnO_2 to determine if the EFG depends on the impurity charge state and, if so, if the value in agreement with the experiment corresponds to the state with lower defect-formation energy. What in fact happens is that the EFGs for both systems do not depend on the impurity charge state nor on the introduction of the U parameter. The explanation of this behavior is that the impurity levels introduced by the Ta atom are delocalized in energy, weakening the incidence of the U parameter on impurity states, having no impact on the EFG prediction. Contrary, in Ta-doped Al_2O_3 the impurity level is basically Ta-5d character and is strongly localized, making the U parameter on these states to influence the origin and behavior of the EFG.

V. CONCLUSIONS

In this work, by means of a combined experimental and *ab initio* approach, applying the TDPAC technique and all-electron DFT electronic structure calculations, we succeeded to dope an α-Al_2O_3 single crystal with a fraction of ^{181}Hf($\rightarrow$ ^{181}Ta) atoms localized at substitutional Al sites *free of defects*, and to characterize the EFG tensor at ^{181}Ta atoms in these sites, both in magnitude and *orientation*. These goals are relevant to correctly compare experimental results with theoretical predictions of the same physical situation. All this enables to show that the inclusion of the U parameter in the *ab initio* predictions to treat the strongly correlated 5d states of Ta when it behaves as a *diluted impurity probe atom* is necessary when the impurity level introduced by it is very localized.

From the *ab initio* point of view, we also show the necessity to increase the dilution of the Ta impurity in this oxide with respect to the dilution sufficient to satisfy the *isolated impurity condition* in the same oxide host but when the impurity is Cd.

The correct assignment of the HFIs and, in consequence the necessity to apply the DFT $+ U$ formalism, would not have been elucidated without performing a defect-formation energy study of the doped systems which indicated the correct charge state of the impurity (Ta^{2+}), enabling to also predict the correct value of the EFG tensor.

This study also showed that a large fraction of ^{181}Hf atoms substitutes Al atoms but with a remaining structural disorder in the far neighborhood of the probe atom. This is the origin of HFIa, the only hyperfine interaction with single-crystalline character already reported in Ref. [44].

Among the structural properties in this doped system, we show that the Ta impurity produces anisotropic outward relaxations for the inequivalent O1 and O2 nearest neighbors. The use of the DFT $+ U$ formalism does not introduce relevant structural changes with respect to DFT, evidencing that the difference in the EFG predictions between both formalisms comes from the modification of the electronic structure description, leading to the described electron density recombination, showing the extraordinary capability of the EFG to detect subtle changes in the electronic structure.

As expected nominally from the oxidation states of Ta^{5+} and Al^{3+}, in effect we demonstrate that Ta introduces a double-donor impurity level in the electronic DOS near the bottom of the conduction band in this wide band-gap semiconductor, highly localized, mainly with Ta-d character, already double ionized (empty) at room temperature. The contribution to the EFG from d orbitals is dominant over the p one when the impurity is not ionized. This Ta-d contribution decreases as the impurity level becomes ionized, while the Ta-p contribution increases. When the impurity level is empty, the Ta-p contribution is the dominant one, leading to the experimentally observed EFG.

Finally, based on the additional EFG *ab initio* calculations using $GGA + U$ for Ta-doped TiO_2 and Ta-doped SnO_2 we demonstrated that the predicted EFGs for both systems do not depend on the introduction of the U parameter since the impurity level introduced by the Ta atom is delocalized in energy, weakening the incidence of the U parameter on the impurity level states, having no impact on the EFG prediction. Contrary, in Ta-doped α-Al_2O_3 the impurity level is strongly localized, affecting the U parameter the impurity states relevant in the origin and behavior of the EFG.

Combined TDPAC and *ab initio*/DFT studies in other Ta-doped oxides are envisaged in order to establish the general conditions that rules this behavior.

[1] M. Springis, P. Kulis, A. Veispals, and I. Tale, Radiat. Meas. **24**, 453 (1995).

[2] J.-F. Boily and J. B. Fein, Geochim. Cosmochim. Acta **60**, 2929 (1996).

[3] C. Verdozzi, D. R. Jennison, P. A. Schultz, M. P. Sears, J. C. Barbour, and B. G. Potter, Phys. Rev. Lett. **80**, 5615 (1998).

[4] T. Dietl, H. Ohno, F. Matsukura, J. Cibert, and D. Ferrand, Science **287**, 1019 (2000).

[5] Y. Matsumoto, M. Murakami, T. Shono, T. Hasegawa, T. Fukumura, M. Kawasaki, P. Ahmet, T. Chikyow, S. Koshihara, and H. Koinuma, Science **291**, 854 (2001).

[6] S. w. Lee, Y.-W. Kim, and H. Chen, Appl. Phys. Lett. **78**, 350 (2001).

[7] Y.-W. Kim, S. W. Lee, and H. Chen, Thin Solid Films **405**, 256 (2002).

[8] J. M. D. Coey, M. Venkatesan, and C. B. Fitzgerald, Nat. Mater. **4**, 173 (2005).

[9] J. Philip, A. Punnoose, B. I. Kim, K. M. Reddy, S. Layne, J. O. Holmes, B. Satpati, P. R. LeClair, T. S. Santos, and J. S. Moodera, Nat. Mater. **5**, 298 (2006).

[10] G. Peleckis, X. Wang, and S. X. Dou, Appl. Phys. Lett. **89**, 022501 (2006).

[11] G. Peleckis, X. L. Wang, and S. X. Dou, Appl. Phys. Lett. **88**, 132507 (2006).

[12] T. K. Sen and M. V. Sarzali, Chem. Eng. J. **142**, 256 (2008).

[13] H. Toyosaki, M. Kawasaki, and Y. Tokura, Appl. Phys. Lett. **93**, 132109 (2008).

[14] S. Nakao, N. Yamada, T. Hitosugi, Y. Hirose, T. Shimada, and T. Hasegawa, Thin Solid Films **518**, 3093 (2010).

[15] S. Qi, F. Jiang, J. Fan, H. Wu, S. B. Zhang, G. A. Gehring, Z. Zhang, and X. Xu, Phys. Rev. B **84**, 205204 (2011).

[16] Y. Muto, S. Nakatomi, N. Oka, Y. Iwabuchi, H. Kotsubo, and Y. Shigesato, Thin Solid Films **520**, 3746 (2012).

[17] J. Zhi, M. Zhou, Z. Zhang, O. Reiser, and F. Huang, Nat. Commun. **12**, 445 (2021).

[18] E. N. Kaufmann and R. J. Vianden, Rev. Mod. Phys. **51**, 161 (1979).

[19] P. Hohenberg and W. Kohn, Phys. Rev. **136**, B864 (1964).

[20] W. Kohn and L. J. Sham, Phys. Rev. **140**, A1133 (1965).

[21] G. Schatz and A. Weidinger, *Nuclear Condensed Matter Physics: Nuclear Methods and Applications* (Wiley, Chichester, England, 1996).

[22] G. K. H. Madsen, P. Blaha, K. Schwarz, E. Sjöstedt, and L. Nordström, Phys. Rev. B **64**, 195134 (2001).

[23] M. S. Moreno, J. Desimoni, A. G. Bibiloni, M. Rentería, C. P. Massolo, and K. Freitag, Phys. Rev. B **43**, 10086 (1991).

[24] M. S. Moreno, J. Desimoni, F. G. Requejo, M. Rentería, A. G. Bibiloni, and K. Freitag, Hyperfine Interact. **62**, 353 (1991).

[25] J. M. Adams and G. L. Catchen, Phys. Rev. B **50**, 1264 (1994).

[26] A. F. Pasquevich, A. G. Bibiloni, C. P. Massolo, M. Rentería, J. A. Vercesi, and K. Freitag, Phys. Rev. B **49**, 14331 (1994).

[27] M. Rentería, F. G. Requejo, A. G. Bibiloni, A. F. Pasquevich, J. Shitu, and K. Freitag, Phys. Rev. B **55**, 14200 (1997).

[28] M. Rentería, A. G. Bibiloni, F. G. Requejo, A. F. Pasquevich, J. Shitu, L. A. Errico, and K. Freitag, Mod. Phys. Lett. B **12**, 819 (1998).

[29] L. A. Errico, M. Rentería, A. F. Pasquevich, A. G. Bibiloni, and K. Freitag, Eur. Phys. J. B **22**, 149 (2001).

[30] A. F. Pasquevich, A. C. Junqueira, A. W. Carbonari, and R. N. Saxena, in *HFI/NQI 2004*, edited by K. Maier and R. Vianden (Springer, Berlin, 2005), pp. 371–375.

[31] L. A. Errico, M. Rentería, A. G. Bibiloni, and K. Freitag, Physica B **389**, 124 (2007).

[32] M. Forker, P. de la Presa, W. Hoffbauer, S. Schlabach, M. Bruns, and D. V. Szabó, Phys. Rev. B **77**, 054108 (2008).

[33] E. L. Muñoz, G. N. Darriba, A. G. Bibiloni, L. A. Errico, and M. Rentería, J. Alloys Compd. **495**, 532 (2010).

[34] E. L. Muñoz, D. Richard, P. D. Eversheim, and M. Rentería, Hyperfine Interact. **197**, 181 (2010).

[35] D. Richard, E. L. Muñoz, L. A. Errico, and M. Rentería, Physica B **407**, 3134 (2012).

[36] J. M. Ramos, T. Martucci, A. W. Carbonari, M. de Souza Costa, R. N. Saxena, and R. Vianden, Hyperfine Interact. **221**, 129 (2013).

[37] D. Richard, G. N. Darriba, E. L. Muñoz, L. A. Errico, and M. Rentería, J. Alloys Compd. **594**, 189 (2014).

[38] D. Richard, M. Rentería, and A. W. Carbonari, Semicond. Sci. Technol. **32**, 085010 (2017).

[39] G. N. Darriba, L. A. Errico, P. D. Eversheim, G. Fabricius, and M. Rentería, Phys. Rev. B **79**, 115213 (2009).

[40] G. N. Darriba, E. L. Muñoz, L. A. Errico, and M. Rentería, J. Phys. Chem. C **118**, 19929 (2014).

[41] D. Richard, G. N. Darriba, E. L. Muñoz, L. A. Errico, P. D. Eversheim, and M. Rentería, J. Phys. Chem. C **120**, 5640 (2016).

[42] M. A. Taylor, R. E. Alonso, L. A. Errico, A. López-García, P. de la Presa, A. Svane, and N. E. Christensen, Phys. Rev. B **82**, 165203 (2010).

[43] M. A. Taylor, R. E. Alonso, L. A. Errico, A. López-García, P. de la Presa, A. Svane, and N. E. Christensen, Phys. Rev. B **85**, 155202 (2012).

[44] M. Rentería, G. N. Darriba, L. A. Errico, E. L. Muñoz, and P. D. Eversheim, Phys. Status Solidi **242**, 1928 (2005).

[45] G. Kresse and D. Joubert, Phys. Rev. B **59**, 1758 (1999).

[46] P. E. Blöchl, Phys. Rev. B **50**, 17953 (1994).

[47] V. I. Anisimov, J. Zaanen, and O. K. Andersen, Phys. Rev. B **44**, 943 (1991).

[48] V. I. Anisimov, I. V. Solovyev, M. A. Korotin, M. T. Czyżyk, and G. A. Sawatzky, Phys. Rev. B **48**, 16929 (1993).

[49] I. V. Solovyev, P. H. Dederichs, and V. I. Anisimov, Phys. Rev. B **50**, 16861 (1994).

[50] P. Darancet, A. J. Millis, and C. A. Marianetti, Phys. Rev. B **90**, 045134 (2014).

[51] M. V. Ivanov, T. V. Perevalov, V. Sh. Aliev, A. A. Gritsenko, and V. V. Kaichev, J. Exp. Theor. Phys. **112**, 1035 (2011).

[52] H. Frauenfelder and R. M. Steffen, in *Alpha-, Beta-, and Gamma-Ray Spectroscopy*, edited by K. Seigbahn (North-Holland Publishing Co., Amsterdam, The Netherlands, 1968).

[53] L. A. Mendoza-Zélis, A. G. Bibiloni, M. C. Caracoche, A. R. Lopéz-García, J. A. Martínez, R. C. Mercader, and A. F. Pasquevich, Hyperfine Interact. **3**, 315 (1977).

[54] D. Wegner, Hyperfine Interact. **23**, 179 (1985).

[55] M. Rentería, A. G. Bibiloni, G. N. Darriba, L. A. Errico, E. L. Muñoz, D. Richard, and J. Runco, Hyperfine Interact. **181**, 145 (2008).

[56] N. J. Stone, At. Data Nucl. Data Tables **90**, 75 (2005).

[57] P. Blaha, K. Schwarz, G. Madsen, D. Kvasnicka, and J. Luitz, *WIEN2k, an Augmented Plane Wave Plus Local Orbitals Program for Calculating Crystal Properties* (Technical Universität, Wien, Austria, 2014).

[58] G. Kresse and J. Furthmüller, Phys. Rev. B **54**, 11169 (1996).

[59] G. Kresse and J. Furthmüller, Comput. Mater. Sci. **6**, 15 (1996).

[60] G. Kresse and J. Hafner, Phys. Rev. B **47**, 558 (1993).

[61] G. Kresse and J. Hafner, Phys. Rev. B **49**, 14251 (1994).

[62] J. P. Perdew, K. Burke, and M. Ernzerhof, Phys. Rev. Lett. **77**, 3865 (1996).

[63] K. Schwarz, C. Ambrosch-Draxl, and P. Blaha, Phys. Rev. B **42**, 2051 (1990).

[64] P. Blaha, K. Schwarz, and P. H. Dederichs, Phys. Rev. B **37**, 2792 (1988).

[65] S. L. Dudarev, G. A. Botton, S. Y. Savrasov, C. J. Humphreys, and A. P. Sutton, Phys. Rev. B **57**, 1505 (1998).

[66] M. Cococcioni and S. de Gironcoli, Phys. Rev. B **71**, 035105 (2005).

[67] G. K. H. Madsen and P. Novák, EPL **69**, 777 (2005).

[68] F. Izumi, H. Asano, H. Murata, and N. Watanabe, J. Appl. Crystallogr. **20**, 411 (1987).

[69] G. N. Darriba, E. L. Muñoz, D. Richard, A. P. Ayala, A. W. Carbonari, H. M. Petrilli, and M. Rentería, Phys. Rev. B **105**, 195201 (2022).

[70] G. N. Darriba, M. Rentería, H. M. Petrilli, and L. V. C. Assali, Phys. Rev. B **86**, 075203 (2012).

[71] G. N. Darriba, E. L. Muñoz, A. W. Carbonari, and M. Rentería, J. Phys. Chem. C **122**, 17423 (2018).

[72] G. N. Darriba, R. Faccio, and M. Rentería, Phys. Rev. B **99**, 195435 (2019).